Rapid spin-resolved single-atom imaging of alkaline-earth fermions

Thies Plassmann,* Leon Schäfer,* Meny Menashes, and Guillaume Salomon†
Institute for Quantum Physics, University of Hamburg, Luruper Chaussee 149, 22761 Hamburg
and The Hamburg Centre for Ultrafast Imaging, University of Hamburg, Luruper Chaussee 149, 22761 Hamburg, Germany

(Received 25 February 2026; accepted 6 October 2026; published 16 November 2026)

Local Hilbert spaces with large dimension are of key interest for quantum information with applications in quantum computing and memories, quantum simulations, and metrology. Thanks to its weak coupling to external perturbations, the large ground-state nuclear spin manifold of fermionic alkaline-earth atoms is an exciting resource to explore for quantum information. Simultaneous single-atom and nuclear-spin-resolved detection, however, remains an outstanding challenge limiting the development of novel quantum computing and simulation schemes beyond qubits. Here, we report on an imaging technique enabling the simultaneous detection of up to four quantum states encoded in the nuclear spin manifold of a single fermionic strontium atom within $\sim$100 µs, with conditional spin-resolved detection fidelities ranging from 93.6% to 99.7%. This technique is further used to track the highly coherent nuclear spin dynamics after a quench, highlighting the potential of this system for quantum information. These results offer fascinating perspectives for quantum science with multielectron atoms ranging from qudit-based quantum computing to quantum simulations of the SU(N) Fermi-Hubbard model.

DOI: 10.1103/t9wk-62kf

I. INTRODUCTION

Impressive progress over the last decade in the engineering, control, and detection of quantum many-body systems at the level of individual constituents holds great promises for quantum computing [1,2], quantum networks [3,4], and quantum-enhanced metrology [5,6] and is bringing quantum simulations to uncharted territories [7–12]. Advanced quantum information science platforms such as trapped ions, superconducting circuits, and cold atoms trapped in optical arrays naturally allow for quantum information processing with a selected number of well-controlled quantum states—two for qubits—or more for so-called qudits.

Trapped ions and superconducting quantum computers and simulators have recently established qudits as promising candidates for fault-tolerant computing and highlighted their potential for quantum simulations [13,14]. Alkali-based cold atom quantum computers with single particle detection and control have so far focused on qubits and demonstrated exciting perspectives for scalability [15–18] and error correction [19]. Improved qubit coherence with alkaline-earth elements [20–22] and multilevel architectures involving both ground and excited states have been reported for quantum computing and metrology using nuclear, clock, and Rydberg states [23–29].

The large Hilbert space dimension $d > 2$ provided by the nuclear spin of ground-state alkaline-earth fermions, with up to $d = 10$ for strontium, is an attractive resource for quantum simulations and computations owing to its weak coupling to environment and SU(N) invariant interactions [30,31]. However, quantum information beyond the two-level paradigm using more than two nuclear spin states remains an outstanding frontier in cold atom systems owing to the absence of high-fidelity nuclear-spin-resolved single-atom detection schemes.

Approaches for nuclear spin state detection based on narrow-line imaging, coherent momentum transfer, and optical Stern-Gerlach separation have been developed for alkaline-earth bulk gases [32–35]. Recently, shelving in long-lived states [20,36] and narrow-line imaging have been exploited in optical tweezer arrays for quantum information processing with nuclear spin qubits [25,37,38]. Despite these advances, the extension of current single-atom spin-resolved detection schemes beyond two nuclear spin states remains challenging thanks to their sequential character. Several additional operations and increased detection times would indeed be required, thereby reducing the fidelity of the imaging process and severely limiting application in quantum simulations and quantum computations such as erasure conversion [23,38,39]. Detection methods involving long-lived excited states [37] are also plagued by trapping-light-induced scattering affecting quantum information stored in the nuclear spin manifold [40], calling for a detection process avoiding their population. Finally, the use of magnetic fields in narrow-line imaging approaches for nuclear-spin resolution is hardly compatible with advanced quantum computing platforms with storage and readout zones [1,19], which require a local detection protocol.

Therefore, a local, rapid single-atom and spin-resolved detection scheme involving all nuclear spins simultaneously

*These authors contributed equally to this work.
†Contact author: guillaume.salomon@uni-hamburg.de

Published by the American Physical Society under the terms of the Creative Commons Attribution 4.0 International license. Further distribution of this work must maintain attribution to the author(s) and the published article's title, journal citation, and DOI.

would be highly promising for harnessing the large nuclear spin manifold of alkaline-earth atoms for qudit-based quantum computing [41–45] and analog quantum simulations with large spin lattice fermions [46–50]. With recent developments in ultrafast imaging of cold atoms [51–56], new opportunities are emerging for nuclear-spin-resolved single-atom detection, paving the way for further breakthroughs in quantum information science with multielectron atoms.

Here, we report on an approach for rapid high-fidelity single-atom and simultaneous nuclear-spin-resolved imaging of ground-state alkaline-earth fermions lasting ∼100 µs. Our technique relies on free space imaging of individual fermionic strontium atoms released from an optical tweezer in combination with a nuclear-spin-state-dependent optical potential realizing a Stern-Gerlach separation for spin-resolved detection. We first demonstrate high-fidelity detection of ^{87}Sr in free space reaching 98.2% for 15 µs imaging time. Next, by flashing for 5 µs a tightly focused laser beam detuned within the hyperfine manifold of the $^3P_1$ state we create an $|m_F|$-dependent force resulting in a discrete spatial atomic distribution after expansion at the focus of a microscope objective. Nuclear-spin-resolved detection fidelities conditioned on detecting an atom ranging from 93.6% to 99.7% for up to four m_F states are reported. As an application, we used this technique to track the coherent nuclear spin dynamics in the ground state after a transverse magnetic field quench, in excellent agreement with theory expectations.

II. RAPID SINGLE-ATOM IMAGING

Our experiments start with a few 10^4 ^{87}Sr atoms trapped in a red magneto-optical trap (MOT) operating on the intercombination line at 689 nm [57]. A 813 nm optical tweezer trap with waist $w_0 = 1.35(8)$ µm and depth $V = k_B \times 1.8$ mK is focused onto the atoms via a microscope objective with 0.55 numerical aperture (Fig. 1). In order to enhance the atom loading efficiency in the tweezer and to confine the atom dynamics at the focus of the microscope objective for low tweezer depths, a 1040 nm elliptical dipole trap propagating along x is used. An overlap of 500 ms of these traps with the red MOT allows to load a few atoms in the optical tweezer. The tweezer depth is then further ramped down in 150 ms to $k_B \times 3.7$ µK resulting in one atom remaining in the trap with about 50% probability, and at a temperature $T = 750(100)$ nK.

Following on the seminal works of Refs. [52,54] with ^{6}Li and ^{168}Er, we first develop and characterize ultrafast imaging in free space for ^{87}Sr. After 5 µs time of flight, two 461 nm counterpropagating beams pulsed in an alternating way (Fig. 1) with intensities $I \sim 20 I_{sat}$, where I_{sat} is the saturation intensity on the blue transition [Fig. 1(c)], are used to induce fluorescence for a variable time t. A few tens of photons collected via the microscope objective are detected on an electron multiplying charge-coupled device (EMCCD) camera (see Appendix B). The recorded images are binarized and low-pass filtered, and the histogram of local maxima displays a characteristic double-peak structure allowing to infer the presence of an atom [Figs. 2(a) and 2(b)]. In order to determine the optimum imaging parameters that both maximize the detection fidelity and minimize the spatial spread of the atomic signal, their respective time evolutions are studied

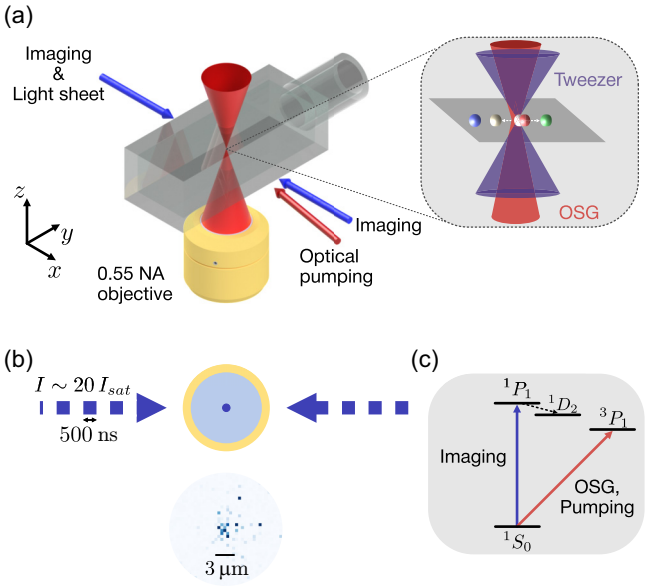


FIG. 1. Experiment overview. (a) Individual ^{87}Sr atoms are trapped in an optical tweezer formed by sending a laser beam through a microscope objective in an ultrahigh-vacuum glass cell. Expanded view: A nuclear-spin-dependent force is created by flashing a linearly polarized optical Stern-Gerlach beam (red, OSG) sent through the microscope objective with a slightly displaced center from the optical tweezer (violet) in the atomic plane. A subsequent free planar evolution in a light sheet dipole trap (gray plane) at the focus of the objective allows to infer the atomic spin from the atom position. (b) Fluorescence is induced by a pair of saturating alternating beams, which are propagating along x and resonant with the blue transition of Sr. A few dozen photons collected via the objective are imaged on an EMCCD camera allowing for the detection of the presence of an atom with high fidelity (bottom experimental image). (c) Strontium level structure. Imaging is performed on the blue transition and the optical Stern-Gerlach beam operates near the red intercombination transition. In order to initialize ground-state atoms in the nuclear spin state $m_F = +9/2$, optical pumping is performed using a σ^+ polarized laser beam on the red intercombination line, in the presence of a guiding magnetic field aligned with its propagation axis (see Appendix A).

[Figs. 2(c) and 2(d)]. Due to momentum diffusion during the scattering process, the standard deviation σ of the atomic fluorescence signal increases with imaging time favoring short exposures. The single-atom detection fidelity reaches a maximum at 98.2(2)% for imaging times between 13.5 and 15 µs, which we attribute to the decay channel toward the $^1D_2$ state (Fig. 1), in good agreement with results reported for ^{88}Sr imaged in a tweezer [39]. The optimum exposure time around 15 µs thus allowed us to reach the highest fidelity with micrometer-scale spatial resolution, which is of prime importance for quantum simulations and computations, and crucial for spin-resolution methods based on spatial separation. We note that fast repumping schemes for the D state exist [58] leaving room for further fidelity improvements.

III. SPIN-RESOLVED SINGLE-ATOM IMAGING

Owing to the weak magnetic sensitivity of nuclear spin states, spatial separation protocols based on magnetic-field

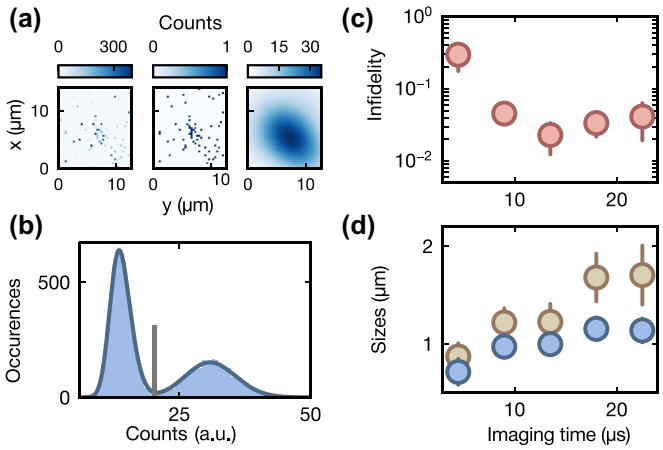


FIG. 2. Rapid imaging of ^{87}Sr in free space. (a) Left to right: Bias-corrected raw, binarized, and low-pass filtered experimental images. (b) Histogram of the low-pass filtered images' maxima, obtained for 15 μs imaging time, displaying a characteristic double-peak structure allowing to distinguish the presence of an atom (high counts) from an empty shot (low-count peak). A fit of the histogram (blue solid line) allows to define a threshold (vertical gray line) and to estimate the fidelity of this assignment. (c) Single-atom detection infidelity as a function of imaging time. (d) Spatial spread of the atomic fluorescence signal as a function of imaging time. The reported sizes are defined as the standard deviations of the fitted anisotropic Gaussian along its major (yellow) and minor (blue) axes. Error bars represent one standard deviation of the mean.

gradients cannot be used for ground-state alkaline-earth atoms, and spin-dependent optical potentials are instead required. Magnetic-field gradients may, however, be an interesting option for large-scale parallel state resolution at the single particle level for species with large magnetic moments such as lanthanides. The use of optical fields for Stern-Gerlach-like separation, on the other hand, offers the advantage of being local, contrary to its magnetic counterpart, which is of importance for quantum computing with separated zones for quantum information processing. In order to simultaneously detect both the presence of an atom and the amplitude $|m_F|$ of its nuclear spin, we develop an optical Stern-Gerlach (OSG) technique operating at the single atom level. A linearly polarized laser beam blue detuned by $\Delta_{\mathrm{OSG}} = 790$ MHz from the $F = 9/2 \rightarrow F' = 11/2$ transition on the intercombination line at 689 nm is used to create a spin-dependent force immediately after release from the optical tweezer [Fig. 3(a)]. The OSG beam is sent through the microscope objective and focused down in the atom plane to a waist $w_{\mathrm{OSG}} = 4.0(2)$ μm with its center horizontally displaced from the tweezer focus by 2 μm, thereby creating a strong optical gradient at the atom position. Owing to the linear polarization of the OSG beam, aligned along x, the vector part of the polarizability tensor vanishes and for the chosen detuning the scalar contribution is small, resulting in an m_F^2-dependent force on the atoms [59]. In this configuration, the maximum number of distinguishable nuclear spin states is thus reduced from 10 to 5. From the current OSG beam power and atom temperature, we estimate that other OSG beam polarization choices would not allow us to resolve significantly more states. This is thus mainly a technical limitation, and generally using the vector polarizability could allow more spin states to be resolved. After a 5 μs pulse of the OSG beam, which is short compared to the excited-state lifetime of 22 μs, the atoms evolve in the light sheet dipole trap confining their motion to the imaging plane. The averaged atomic fluorescence signal after an in-plane expansion $T_{\mathrm{exp}} = 94$ μs clearly reveals four distinct regions where the atoms can appear, with a maximum splitting between the outermost ones of 25 μm [Fig. 3(b), left and Fig. 3(d), top]. When optically pumping the trapped atoms to $m_F = +9/2$ using light resonant with the $F = 9/2 \rightarrow F' = 9/2$ intercombination transition prior to Stern-Gerlach separation (see Appendix A), only the upper region is observed [Fig. 3(b), right]. Given that $|m_F| = 5/2$ is barely affected by the OSG beam, we could attribute $|m_F|$ states to the three regions observed from top to bottom to $|m_F| = 9/2, 7/2, 5/2$ and the bottom one to $|m_F| = 3/2, 1/2$, which are not resolved for the chosen experimental parameters (see Appendix C). Gaussian modeling of the four individual atom locations observed is used to assign region boundaries [Fig. 3(c)] and determine spin detection fidelities conditioned on detecting an atom [Fig. 3(d)] of 99.70(6)% for $|m_F| = 9/2$, 98.7(2)% for $|m_F| = 7/2$, 93.6(8)% for $|m_F| = 5/2$, and 94.6(7)% for $|m_F| = 1/2, 3/2$ (see Appendix D). We occasionally detect two atoms, suggesting that our detection is compatible with initial tweezer occupations higher than one, and we leave for future work a study beyond the single atom level.

IV. COHERENT NUCLEAR SPIN DYNAMICS

As a benchmark for our method, we track the coherent nuclear spin dynamics after a magnetic field quench [60]. The individual atoms are first pumped to the stretched $m_F = +9/2$ state in the presence of a guiding magnetic field pointing along x (Fig. 1). The magnetic field is then quenched in the transverse vertical direction z and held for a variable time t, inducing nuclear spin dynamics before detection. Coherent oscillations of the m_F populations on a 1 s timescale are observed (Fig. 4) in excellent agreement with theory expectations (see Appendix D). This result both demonstrates coherent control of the nuclear spin manifold of ^{87}Sr at the single particle level and experimentally justifies the assignment of the $|m_F|$ regions [Figs. 3(b) and 3(c)]. The nuclear spin dynamics is found to remain coherent with no visible decay of contrast of the oscillations up to 500 ms without dynamical decoupling, highlighting the potential of the nuclear spin manifold for robust quantum information storage [20,21,25].

V. OUTLOOK AND CONCLUSIONS

Before discussing the scalability of our technique to larger systems, it is instructive to consider the various contributions to the measured $|m_F|$-class sizes, which directly affect the required spacing for high-fidelity imaging in arrays. The observed different sizes of the four regions [Fig. 3(d)] are attributed to a lensing effect induced by the OSG beam Gaussian profile during the pulse (see Appendix C and Fig. 5(b) of Appendix A). The latter could in principle be mitigated by wavefront shaping of the OSG beam using a spatial light modulator. The relatively high temperature of the atoms,

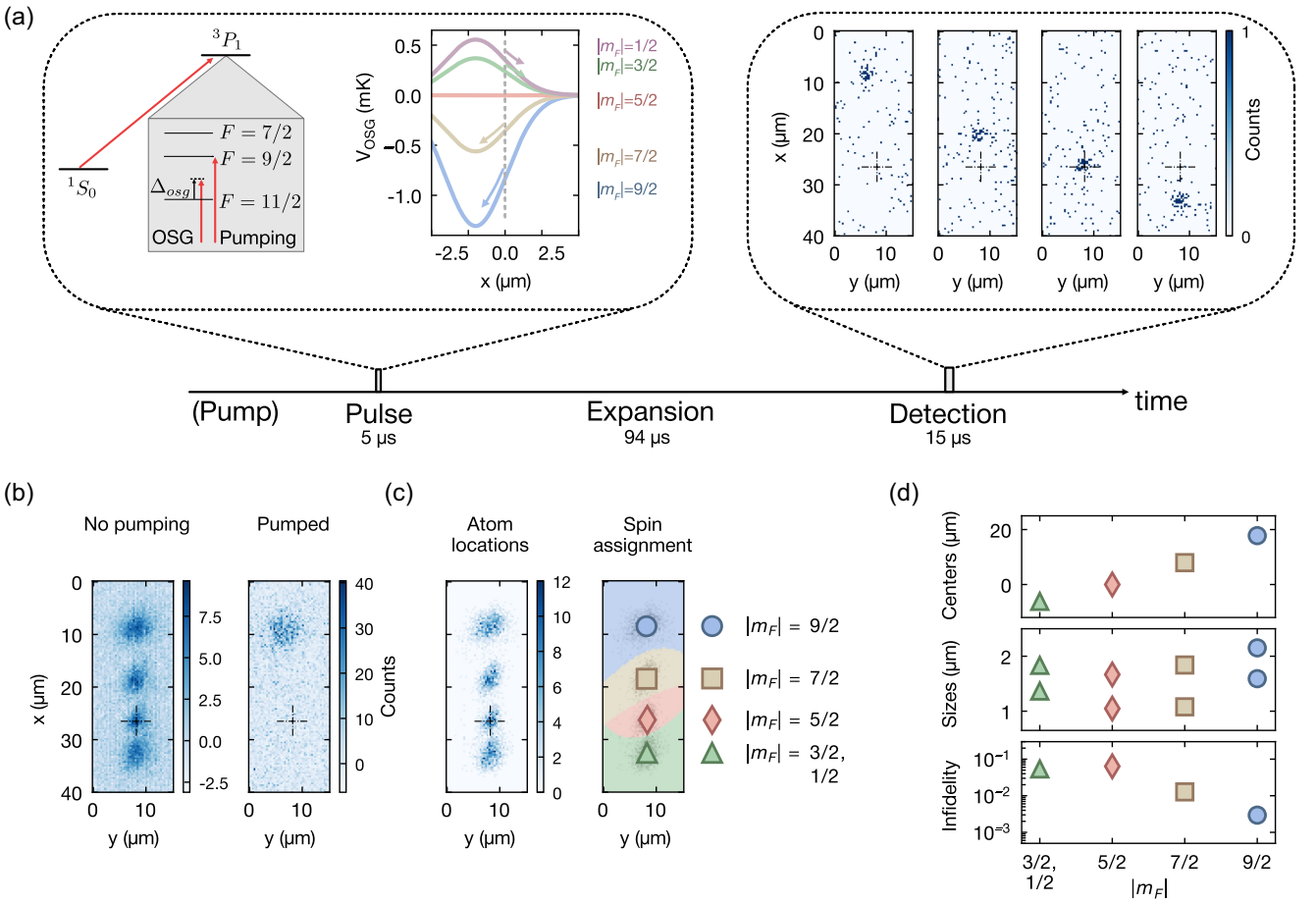


FIG. 3. Spin-resolved imaging. (a) An optical Stern-Gerlach beam is detuned with $\Delta_{\mathrm{OSG}} = +790$ MHz from the $F = 9/2 \rightarrow F' = 11/2$ red transition creating an $|m_F|$-dependent potential gradient at the atom location (left expanded view, vertical dashed gray line). After illuminating the atom for 5 μs with the OSG beam, the accumulated $|m_F|$-dependent momentum change is mapped during an in-plane expansion into spatially distinct locations detected by fluorescence imaging (right expanded view: binarized images of individual realizations). The cross indicates the tweezer position. (b) Averaged fluorescence picture with one atom (left) displaying a four-region structure, whereas after optical pumping to $m_F = +9/2$ only one region remains (right). (c) Left: Sum of all single atom locations in 3738 experimental realizations containing an atom. The spin region assignment is determined from a four-component Gaussian mixture modeling of the atom locations (see Appendix C). (d) Top: Distance of the spin regions centers from the tweezer position. Middle: Major and minor sizes of the four Gaussian distributions used in the model. Bottom: $|m_F|$ assignment infidelities.

corresponding to a mean radial vibrational quantum number $\bar{n} \simeq 3$, also induces a non-negligible spatial distribution increase during the in-plane expansion (see Appendix C and Fig. 5 of Appendix). This effect can be strongly suppressed in future works by performing sideband cooling near the ground state [61,62]. The last contribution to the observed sizes is the spatial spread during imaging, which can be reduced by using shorter exposure times. Improvements can clearly be foreseen here in order to approach exposure times in the 5 μs range as reported with Yb and Er [54,56] since the transmission efficiency of our imaging system from the objective to the camera currently is only ∼25%. A further intriguing possibility to suppress the spatial spread during imaging would involve recapturing atoms in tweezers after expansion [63], which is, however, left to future studies.

A natural strategy to scale the current OSG technique to several particles would use dynamical optical tweezer arrays formed with crossed acousto-optic deflectors, allowing to realize both one- and two-dimensional systems and perform rapid transport of atoms [17,18,64]. Based on the results presented in Fig. 3, using a square array spacing dynamically tuned for detection to 18 μm and implementing the OSG separation along the diagonal with one OSG beam per site, systems up to ∼200 atoms could be investigated in our experiment. At typical speeds of 0.1−0.3 μm/μs for atom transport in optical tweezers [17,18,64,65], we estimate that scaling up the array to such spacing would add about a millisecond to the total detection time. With improved temperature and shorter imaging time, a further reduction of the required array spacing, and corresponding increase in atom number and imaging speed, can be envisioned.

In summary, we have presented here a rapid high-fidelity single-atom and spin resolution technique generically applicable to alkaline-earth fermions and other multielectron atoms, which opens several avenues for quantum information science. Combined with optical arrays with tunable spacing such as accordion optical lattices [66] and programmable optical tweezer arrays [67], this technique will, for example, allow for

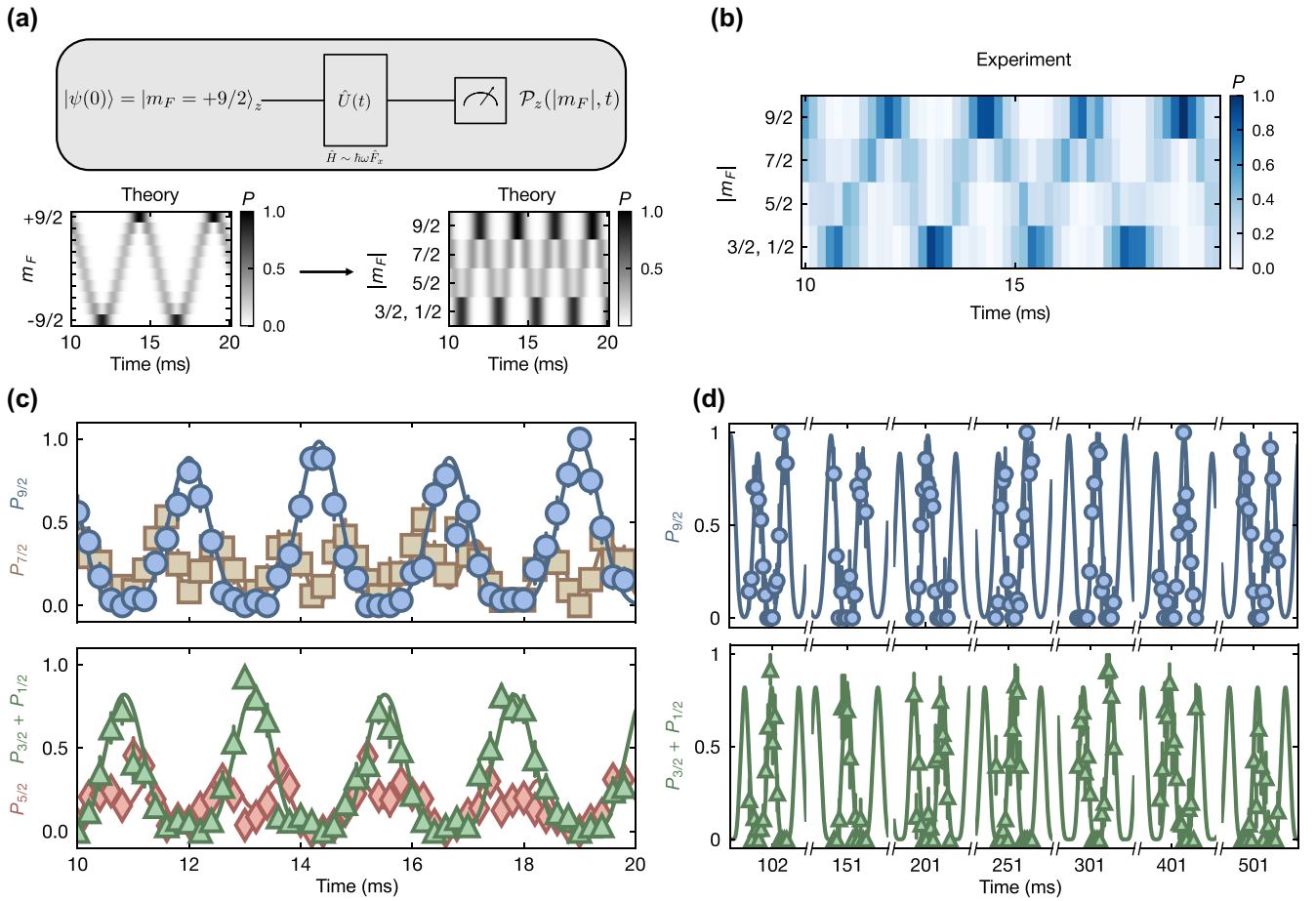


FIG. 4. Coherent spin dynamics. (a) Top: Atoms initialized in the $m_F = +9/2$ state evolve under a near-transverse magnetic field for a time t before detection, which corresponds to a unitary evolution under a Hamiltonian $\hat{H} \sim \hat{F}_x$, where $\hat{F}$ is a spin-9/2 operator. Bottom: Coherent spin dynamics theory expectations (left) induced by the field during the quench (see Appendix D) and as would be measured by our detection method only sensitive to $|m_F|$ (right). (b) Experimental time evolution of the $|m_F|$ populations. (c) Time evolutions of the $|m_F| = 9/2$ (blue dots), $|m_F| = 7/2$ (yellow squares), $|m_F| = 5/2$ (red diamonds), and $|m_F| = 3/2, 1/2$ (green triangles) populations and theory expectations (solid lines). (d) Long-time population dynamics for $|m_F| = 9/2$ (blue dots) and $|m_F| = 3/2, 1/2$ (green triangles) and theory expectations (solid lines). Error bars represent one standard deviation of the mean.

spin-resolved quantum gas microscopy of the SU(N) Fermi-Hubbard model [68] and of dipolar spin mixtures as realized with lanthanides [66,69–71]. Being compatible with advanced quantum computing architectures [25], the reported results should further allow to leverage the large nuclear spin Hilbert space of alkaline-earth atoms for quantum information processing. In particular, it will be exciting to use it in the future to explore qudit-based quantum computing [41,42,45], novel mid-circuit measurements, and erasure protocols [23,39] and to develop novel quantum error correcting codes tailored to multilevel systems.

ACKNOWLEDGMENTS

We thank F. Scazza, L. Tarruell, S. Buob, and T. Rubio Abadal for insightful discussions, and H. Moritz, S. Häfele, and C. Salomon for critical reading of the manuscript. This project has received funding from the European Research Council (ERC) under the European Union's Horizon 2020 research and innovation program (Grant Agreement No. 852236, "FLATBANDS"). T.P., L.S., and G.S. acknowledge funding support from the Cluster of Excellence "CUI: Advanced Imaging of Matter" of the Deutsche Forschungsgemeinschaft (DFG)–EXC 2056 – Project ID 390715994.

T.P. and L.S. contributed equally to this work. T.P., L.S., M.M., and G.S. planned and conducted the study. T.P. and L.S. performed the data acquisition and G.S. supervised the study. All authors contributed to the analysis of the results presented here and to the writing of the manuscript.

DATA AVAILABILITY

The data that support the findings of this article are openly available [72].

APPENDIX A: SINGLE-ATOM PREPARATION

Our experimental sequence starts by collecting for a few seconds ^{87}Sr atoms, which have a nuclear spin $I = 9/2$ and

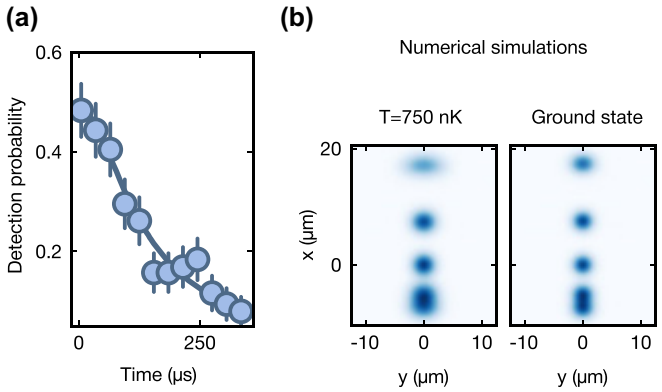


FIG. 5. (a) Single-atom detection probability as a function of hold time with tweezer off. Solid line: Classical Monte Carlo expectation for a temperature of 750 nK. (b) Numerical simulation results of the optical Stern-Gerlach detection method for a cropped thermal distribution (36 lowest energy states) in the tweezer at $T = 750$ nK (left), and for the harmonic oscillator ground state (right), taking into account the spatial resolution of our detection due to atomic motion during imaging. As seen in the experiment, only four regions are well defined and both the center distances of the $|m_F|$ regions and their elliptical shape are in good agreement with the experiment. From a comparison with ground-state expectations, the spin detection fidelities for the experimental settings in this article were limited by the initial atomic temperature, and the absence of visible splitting between $|m_F| = 3/2$ and $|m_F| = 1/2$ was attributed to the atomic motion during imaging.

hence total spin $F = 9/2$ in their ground state, from a commercial cold atom beam source (AOSense) in a blue MOT operating on the broad ${}^1S_0 \rightarrow {}^1P_1$ transition in an uncoated ultrahigh-vacuum glass cell. The MOT consists of three pairs of retroreflected beams with 5 mm waist and each with peak intensities of $0.3 \times I^B_{\rm sat}$, where $I^B_{\rm sat} = 40\,{\rm mW/cm^2}$ is the saturation intensity on the blue transition. These beams are detuned by $\Delta = -1.2 \times \Gamma_B$ from the excited state $F' = 11/2$, where Γ_B is the linewidth of the 461 nm blue transition, and operate in the presence of a quadrupolar magnetic field with a gradient of 46 G/cm along the strong x axis. During the MOT loading phase, atoms accumulate in the magnetically trappable states of the ${}^3P_2$ manifold [57]. At the end of the blue MOT, repumpers operating at 707 and 679 nm, resonant with the ${}^3P_2 \rightarrow 6s\,{}^3S_1$ and ${}^3P_0 \rightarrow 6s\,{}^3S_1$, are turned on to pump atoms back to the ground state. Simultaneously, the magnetic-field gradient is ramped down to 3 G/cm and three pairs of retroreflected red-detuned red MOT beams operating on the intercombination line ${}^1S_0 \rightarrow {}^3P_1$ are turned on. Each beam, with 3.5 mm waist and peak intensity of $3400 \times I^R_{\rm sat}$, where $I^R_{\rm sat} = 3\,\mu{\rm W/cm^2}$, contains two frequencies to address both the $F = 9/2 \rightarrow F' = 11/2$ (MOT) and the $F = 9/2 \rightarrow F' = 9/2$ (stirring) transitions [57]. These beams are frequency modulated using a triangular shape spanning 4 MHz with a 50 μs period during a first capture phase. After 25 ms of such frequency modulation, the span is linearly decreased to zero in 75 ms. The laser power is further reduced in 150 ms to $\sim 100 \times I^R_{\rm sat}$ and its frequency for the MOT transition ramped to a detuning $\Delta_r \simeq -650$ kHz while atoms start to accumulate in the 1040 nm light sheet dipole trap. The light sheet dipole trap propagating along x is elliptical with waists 20 μm along z and 200 μm along y, and a depth of $k_{\rm B} \times 60$ μK. The 813 nm tweezer trap with 1.35(8) μm waist and a depth $k_{\rm B} \times 1.8$ mK is switched on at the start of the red MOT sequence. After 500 ms holding time, both the red MOT beams and light sheet trap powers are ramped down to zero in 100 ms such that only atoms trapped in the tweezer remain. In order to pump atoms to $m_F = +9/2$, a guiding magnetic field of about 2 G pointing along the pumping beam propagation axis is turned on, and the tweezer power ramped down in 100 ms by a factor of 10 in order to decrease off-resonant scattering from the trap. Optical pumping is performed during 54 ms using a frequency-modulated σ^+ polarized laser beam spanning ~6 MHz with a 27 μs period, and with $90 \times I^R_{\rm sat}$ peak intensity, allowing for efficient pumping in the presence of excited-state tensor light shift from the tweezer trap. In order to reduce the momentum spread of the atoms during detection, the tweezer power is reduced by another factor 50 in 150 ms, and the light sheet dipole trap is simultaneously ramped up to a depth of $k_{\rm B} \times 6$ μK providing further longitudinal confinement at such low tweezer depth. Using a sample and hold stabilization of the tweezer power, its final depth is found to fluctuate with 2.5% standard deviation. At these final settings, the tweezer trap remains filled with either a single atom or none with about 50% probability. The temperature of the atoms is estimated using a release-recapture method [73]. It consists in switching off the tweezer for a variable time t before turning it back on and measuring the probability to detect an atom using free space imaging [Fig. 5(a)]. A comparison with classical Monte Carlo predictions [73] allows to estimate the temperature $T = 750(100)$ nK [Fig. 5(a)].

APPENDIX B: FAST IMAGING

The free space imaging sequence reported in the main text is developed for strontium following on the seminal works of Refs. [52,54]. Freely expanding atoms in the light sheet dipole trap are illuminated with two alternating and saturating counterpropagating beams with typical peak intensities $I = 20\,I_{\rm sat}$ in the presence of a small guiding magnetic field of 80 mG along x. The two imaging beams, linearly polarized along y, are turned on during 500 ns in opposite phase with minimal time overlap in order to avoid fast momentum spread [54]. Scattered photons from the atoms are collected through a custom microscope objective (SpecialOptics) with numerical aperture 0.55 that transmits 50% of blue light. Two dichroic mirrors in the imaging path after the objective are used to split the blue wavelength from the 813 nm tweezer light and the OSG 689 nm light, and two bandpass filters are used for stray light filtering in front of the sensor. The collected blue light is focused onto an EMCCD camera (Andor Ixon Ultra 897) with total magnification of 47.8 for the full imaging system. For single-photon sensitivity, we operate the camera at high gain. At EM gain of 1000, we measure a gain over readout noise $g/\sigma_{\rm read} = 35$ allowing to work in the single-photon counting regime [52].

For further analysis, the bias-corrected images are binarized using a single-photon detection threshold at $6.5 \times \sigma_{\rm read}$ effectively making the readout noise of the camera negligible and minimizing the influence of the clock-induced charge

(CIC) noise of the sensor, measured to be 2% per pixel for our camera settings, while keeping more than 80% of the atomic photon signal [52,54]. The binarized images are further low-pass filtered taking advantage of the different spatial distributions of CIC and atomic signal using an elliptical Gaussian kernel with sizes $\sigma = 8,\ 10.4$ pixels along its principal axis [Fig. 2(a)]. The histogram of the maxima of the binarized low-pass filtered images displays a characteristic double-peak structure corresponding to the presence or absence of an atom allowing to assign a threshold for single-atom detection [Fig. 2(b)] and to estimate the fidelity of the imaging process. The histograms are fitted using the sum of one skewed Gaussian for the peak at low counts (zero atom) and a skewed Gaussian plus an offset for the one-atom peak. The offset between the peak at low counts and the peak at high counts models the decay toward the long-lived dark state $^1D_2$ during the imaging [54]. An atom that has decayed from $^1P_1$ to $^1D_2$ is indeed dark for the rest of the imaging sequence and, given that this decay can happen at any time, it appears as a homogeneous distribution of counts connecting the two peaks in the histogram. The optimum count threshold for single atom assignment is obtained when the two modeled peak distributions intersect allowing to estimate a fidelity of 98.2(2)% for 15 µs imaging time.

APPENDIX C: OPTICAL STERN-GERLACH

The laser used to create the Stern-Gerlach optical potential is offset locked to our main red MOT laser, whose frequency is stabilized onto a cavity with 256 000 finesse leading to a sub-kilohertz linewidth. The OSG laser is detuned by +790 MHz from the $F = 9/2 \rightarrow F' = 11/2$ red transition and is linearly polarized along x. The vector polarizability contribution vanishes for linear polarization and the spin-dependent force is provided by the tensor contribution of the polarizability that scales as m_F^2, thereby reducing the number of different nuclear spin states, which could in principle be detected from 10 to 5. For this detuning, the ground-state scalar polarizability is $\alpha_s = 7.2 \times 10^3$ a.u. and the tensor polarizability is $\alpha_t = 42.5 \times 10^3$ a.u. On the experiment, owing to the relatively large atomic spatial spread during imaging the distributions of $|m_F| = 3/2$ and $|m_F| = 1/2$ are strongly overlapping, further reducing the number of different states that can be identified to four for our imaging settings [Fig. 5(b)]. The OSG beam is projected onto the atoms via the objective to a waist of 4.0(2) µm and power of 2.8 mW. The waist of this beam was experimentally determined by using it as a red-detuned dipole trap and measuring the trapping frequency for the ^{88}Sr isotope. The power fluctuations of the OSG beam are kept below 2.5% (standard deviation) using a sample and hold stabilization method. The relative alignment of the OSG beam and the tweezer trap is controlled by maximizing the accumulated momentum kick, which is mapped in the distance from the tweezer after 94 µs in-plane expansion. At the start of the OSG pulse and for the free expansion, the light sheet dipole trap depth is increased to its maximal value in order to prevent kicking atoms out of focus. We observe slow drifts of the relative tweezer and OSG beam alignment necessitating slight realignments on a weekly timescale. In order to faithfully image the initial spin distribution, it is important to align the polarization of the OSG beam and the magnetic field quantization axis prior to detection. This is achieved by optimizing the fraction of atoms detected in the $|m_F| = 9/2$ region after optical pumping.

APPENDIX D: ANALYSIS OF SPIN-RESOLVED DATA

Assigning an atom to an $|m_F|$ region in an individual experimental realization with OSG detection necessitates first to define the atom location based on the fluorescence signal collected on the camera. We use the peak of the low-pass filtered images to define the atom location in a single shot [52]. The next step requires to model the atom location distributions observed, which reduces to a classification problem. Since we experimentally observe four distinct regions, we fit a Gaussian mixture model [74] to the measured atom locations in order to estimate the probability densities of the different $|m_F|$ regions. From the four fitted Gaussian probability distributions (pdf), the optimal boundaries are defined where the pdfs are equal allowing for each realization to assign an atom to an $|m_F|$ region based on the highest pdf at this location. The spin assignment infidelities stated in the text are estimated from the overlap of the probability density functions extracted from the Gaussian mixture model distributions and represent the sum of false positives and missed detections for each region. The error bars on the fidelities denote one standard error of the mean and are obtained from bootstrapping the data. The elliptical shapes of the atom location distributions and region centers are well reproduced from numerical simulations of the atom dynamics in the OSG beam during the pulse and its subsequent free propagation [Fig. 5(b)]. The good agreement between experiment and numerics allows to identify the temperature of the atoms as the current main limitation for the fidelities reported in this work.

During the quench dynamics experiments, two orthogonal pairs of coils in a Helmholtz-like configuration are used to control the magnetic field. The first one defining the quantization axis prior to the quench has its strong axis aligned along x and its current is kept constant during the time evolution. The second pair of coils used for the quench has its main axis aligned along z and is turned on and off on a submillisecond timescale for the quench. Theory modeling of the coherent dynamics induced by the magnetic field quench is based on exact diagonalization of the dynamics of a spin $F = 9/2$ in the presence of the magnetic fields induced by the two pairs of coils after the state was initialized in the $m_F = +9/2$ state along the quantization axis prior to detection. We find that a quench field of 1.158 G with a $1/e$ rise time of 0.3 ms and an initial guiding field of 80 mG capture well the full experimental coherent dynamics. These field values agree within 5 mG with independent calibrations based on spectroscopy on the red intercombination line. Stray magnetic field variations of a few milligauss can significantly change the angle between the initial quantization basis and the detection basis provided by the OSG beam, due to the relatively weak guiding magnetic field used prior to the quench. We find that for this measurement set spanning several days an angle of 5°, well within experimental uncertainties, allows to reproduce well our data.

[1] D. Bluvstein, S. J. Evered, A. A. Geim, S. H. Li, H. Zhou, T. Manovitz, S. Ebadi, M. Cain, M. Kalinowski, D. Hangleiter, *et al.*, Logical quantum processor based on reconfigurable atom arrays, Nature (London) **626**, 58 (2024).

[2] F. Arute, K. Arya, R. Babbush, D. Bacon, J. C. Bardin, R. Barends, R. Biswas, S. Boixo, F. G. S. L. Brandao, D. A. Buell, *et al.*, Quantum supremacy using a programmable superconducting processor, Nature (London) **574**, 505 (2019).

[3] L. Hartung, M. Seubert, S. Welte, E. Distante, and G. Rempe, A quantum-network register assembled with optical tweezers in an optical cavity, Science **385**, 179 (2024).

[4] B. Grinkemeyer, E. Guardado-Sanchez, I. Dimitrova, D. Shchepanovich, G. E. Mandopoulou, J. Borregaard, V. Vuletić, and M. D. Lukin, Error-detected quantum operations with neutral atoms mediated by an optical cavity, Science **387**, 1301 (2025).

[5] R. Finkelstein, R. B.-S. Tsai, X. Sun, P. Scholl, S. Direkci, T. Gefen, J. Choi, A. L. Shaw, and M. Endres, Universal quantum operations and ancilla-based read-out for tweezer clocks, Nature (London) **634**, 321 (2024).

[6] A. Cao, W. J. Eckner, T. Lukin Yelin, A. W. Young, S. Jandura, L. Yan, K. Kim, G. Pupillo, J. Ye, N. Darkwah Oppong, and A. M. Kaufman, Multi-qubit gates and Schrödinger cat states in an optical clock, Nature (London) **634**, 315 (2024).

[7] M. Xu, L. H. Kendrick, A. Kale, Y. Gang, C. Feng, S. Zhang, A. W. Young, M. Lebrat, and M. Greiner, A neutral-atom Hubbard quantum simulator in the cryogenic regime, Nature (London) **642**, 909 (2025).

[8] M. Qiao, G. Emperauger, C. Chen, L. Homeier, S. Hollerith, G. Bornet, R. Martin, B. Gély, L. Klein, D. Barredo, S. Geier, N.-C. Chiu, F. Grusdt, A. Bohrdt, T. Lahaye, and A. Browaeys, Realization of a doped quantum antiferromagnet in a Rydberg tweezer array, Nature (London) **644**, 889 (2025).

[9] S. J. Evered, M. Kalinowski, A. A. Geim, T. Manovitz, D. Bluvstein, S. H. Li, N. Maskara, H. Zhou, S. Ebadi, M. Xu, J. Campo, M. Cain, S. Ostermann, S. F. Yelin, S. Sachdev, M. Greiner, V. Vuletić, and M. D. Lukin, Probing the Kitaev honeycomb model on a neutral-atom quantum computer, Nature (London) **645**, 341 (2025).

[10] P. Sompet, S. Hirthe, D. Bourgund, T. Chalopin, J. Bibo, J. Koepsell, P. Bojović, R. Verresen, F. Pollmann, G. Salomon, C. Gross, T. A. Hilker, and I. Bloch, Realizing the symmetry-protected Haldane phase in Fermi–Hubbard ladders, Nature (London) **606**, 484 (2022).

[11] M. Meth, J. Zhang, J. F. Haase, C. Edmunds, L. Postler, A. J. Jena, A. Steiner, L. Dellantonio, R. Blatt, P. Zoller, T. Monz, P. Schindler, C. Muschik, and M. Ringbauer, Simulating two-dimensional lattice gauge theories on a qudit quantum computer, Nat. Phys. **21**, 570 (2025).

[12] K. J. Satzinger, Y.-J Liu, A. Smith, C. Knapp, M. Newman, C. Jones, Z. Chen, C. Quintana, X. Mi, A. Dunsworth, *et al.*, Realizing topologically ordered states on a quantum processor, Science **374**, 1237 (2021).

[13] M. Ringbauer, M. Meth, L. Postler, R. Stricker, R. Blatt, P. Schindler, and T. Monz, A universal qudit quantum processor with trapped ions, Nat. Phys. **18**, 1053 (2022).

[14] B. L. Brock, S. Singh, A. Eickbusch, V. V. Sivak, A. Z. Ding, L. Frunzio, S. M. Girvin, and M. H. Devoret, Quantum error correction of qudits beyond break-even, Nature (London) **641**, 612 (2025).

[15] F. Gyger, M. Ammenwerth, R. Tao, H. Timme, S. Snigirev, I. Bloch, and J. Zeiher, Continuous operation of large-scale atom arrays in optical lattices, Phys. Rev. Res. **6**, 033104 (2024).

[16] M. A. Norcia, H. Kim, W. B. Cairncross, M. Stone, A. Ryou, M. Jaffe, M. O. Brown, K. Barnes, P. Battaglino, T. C. Bohdanowicz, *et al.*, Iterative assembly of ^{171}Yb atom arrays with cavity-enhanced optical lattices, PRX Quantum **5**, 030316 (2024).

[17] H. J. Manetsch, G. Nomura, E. Bataille, X. Lv, K. H. Leung, and M. Endres, A tweezer array with 6,100 highly coherent atomic qubits, Nature (London) **647**, 60 (2025).

[18] N.-C. Chiu, E. C. Trapp, J. Guo, M. H. Abobeih, L. M. Stewart, S. Hollerith, P. L. Stroganov, M. Kalinowski, A. A. Geim, S. J. Evered, S. H. Li, X. Lyu, L. M. Peters, D. Bluvstein, T. T. Wang, M. Greiner, V. Vuletić, and M. D. Lukin, Continuous operation of a coherent 3,000-qubit system, Nature (London) **646**, 1075 (2025).

[19] D. Bluvstein, A. A. Geim, S. H. Li, S. J. Evered, J. P. Bonilla Ataides, G. Baranes, A. Gu, T. Manovitz, M. Xu, M. Kalinowski, *et al.*, A fault-tolerant neutral-atom architecture for universal quantum computation, Nature (London) **649**, 39 (2026).

[20] K. Barnes, P. Battaglino, B. J. Bloom, K. Cassella, R. Coxe, N. Crisosto, J. P. King, S. S. Kondov, K. Kotru, S. C. Larsen, *et al.*, Assembly and coherent control of a register of nuclear spin qubits, Nat. Commun. **13**, 2779 (2022).

[21] S. Ma, A. P. Burgers, G. Liu, J. Wilson, B. Zhang, and J. D. Thompson, Universal gate operations on nuclear spin qubits in an optical tweezer array of ^{171}Yb atoms, Phys. Rev. X **12**, 021028 (2022).

[22] A. Jenkins, J. W. Lis, A. Senoo, W. F. McGrew, and A. M. Kaufman, Ytterbium nuclear-spin qubits in an optical tweezer array, Phys. Rev. X **12**, 021027 (2022).

[23] S. Ma, G. Liu, P. Peng, B. Zhang, S. Jandura, J. Claes, A. P. Burgers, G. Pupillo, S. Puri, and J. D. Thompson, High-fidelity gates and mid-circuit erasure conversion in an atomic qubit, Nature (London) **622**, 279 (2023).

[24] J. A. Muniz, M. Stone, D. T. Stack, M. Jaffe, J. M. Kindem, L. Wadleigh, E. Zalys-Geller, X. Zhang, C.-A. Chen, M. A. Norcia, *et al.*, High-fidelity universal gates in the ^{171}Yb ground-state nuclear-spin qubit, PRX Quantum **6**, 020334 (2025).

[25] J. W. Lis, A. Senoo, W. F. McGrew, F. Rönchen, A. Jenkins, and A. M. Kaufman, Midcircuit operations using the *omg* architecture in neutral atom arrays, Phys. Rev. X **13**, 041035 (2023).

[26] S. Pucher, V. Klüsener, F. Spriestersbach, J. Geiger, A. Schindewolf, I. Bloch, and S. Blatt, Fine-structure qubit encoded in metastable strontium trapped in an optical lattice, Phys. Rev. Lett. **132**, 150605 (2024).

[27] G. Unnikrishnan, P. Ilzhöfer, A. Scholz, C. Hölzl, A. Götzelmann, R. K. Gupta, J. Zhao, J. Krauter, S. Weber, N. Makki, H. P. Büchler, T. Pfau, and F. Meinert, Coherent control of the fine-structure qubit in a single alkaline-earth atom, Phys. Rev. Lett. **132**, 150606 (2024).

[28] M. Ammenwerth, H. Timme, F. Gyger, R. Tao, I. Bloch, and J. Zeiher, Realization of a fast triple-magic all-optical qutrit in ^{88}Sr, Phys. Rev. Lett. **135**, 143401 (2025).

[29] R. B.-S. Tsai, X. Sun, A. L. Shaw, R. Finkelstein, and M. Endres, Benchmarking and fidelity response theory of high-fidelity Rydberg entangling gates, PRX Quantum **6**, 010331 (2025).

[30] F. Scazza, C. Hofrichter, M. Höfer, P. C. De Groot, I. Bloch, and S. Fölling, Observation of two-orbital spin-exchange interactions with ultracold SU(N)-symmetric fermions, Nat. Phys. **10**, 779 (2014).

[31] X. Zhang, M. Bishof, S. L. Bromley, C. V. Kraus, M. S. Safronova, P. Zoller, A. M. Rey, and J. Ye, Spectroscopic observation of SU(N)-symmetric interactions in Sr orbital magnetism, Science **345**, 1467 (2014).

[32] S. Taie, Y. Takasu, S. Sugawa, R. Yamazaki, T. Tsujimoto, R. Murakami, and Y. Takahashi, Realization of a SU(2) × SU(6) system of fermions in a cold atomic gas, Phys. Rev. Lett. **105**, 190401 (2010).

[33] S. Stellmer, R. Grimm, and F. Schreck, Detection and manipulation of nuclear spin states in fermionic strontium, Phys. Rev. A **84**, 043611 (2011).

[34] F. Leroux, K. Pandey, R. Rehbi, F. Chevy, C. Miniatura, B. Grémaud, and D. Wilkowski, Non-Abelian adiabatic geometric transformations in a cold strontium gas, Nat. Commun. **9**, 3580 (2018).

[35] P. Bataille, A. Litvinov, I. Manai, J. Huckans, F. Wiotte, A. Kaladjian, O. Gorceix, E. Maréchal, B. Laburthe-Tolra, and M. Robert-de-Saint-Vincent, Adiabatic spin-dependent momentum transfer in an SU(N) degenerate Fermi gas, Phys. Rev. A **102**, 013317 (2020).

[36] A. Senoo, A. Baumgärtner, J. W. Lis, G. M. Vaidya, Z. Zeng, G. Giudici, H. Pichler, and A. M. Kaufman, High-fidelity entanglement and coherent multi-qubit mapping in an atom array, Nat. Phys. **22**, 903 (2026).

[37] W. Huie, L. Li, N. Chen, X. Hu, Z. Jia, W. K. C. Sun, and J. P. Covey, Repetitive readout and real-time control of nuclear spin qubits in ^{171}Yb atoms, PRX Quantum **4**, 030337 (2023).

[38] M. A. Norcia, W. B. Cairncross, K. Barnes, P. Battaglino, A. Brown, M. O. Brown, K. Cassella, C.-A. Chen, R. Coxe, D. Crow, *et al.*, Midcircuit qubit measurement and rearrangement in a ^{171}Yb atomic array, Phys. Rev. X **13**, 041034 (2023).

[39] P. Scholl, A. L. Shaw, R. B.-S. Tsai, R. Finkelstein, J. Choi, and M. Endres, Erasure conversion in a high-fidelity Rydberg quantum simulator, Nature (London) **622**, 273 (2023).

[40] S. Dörscher, R. Schwarz, A. Al-Masoudi, S. Falke, U. Sterr, and C. Lisdat, Lattice-induced photon scattering in an optical lattice clock, Phys. Rev. A **97**, 063419 (2018).

[41] E. O. Kiktenko, A. S. Nikolaeva, and A. K. Fedorov, *Colloquium*: Qudits for decomposing multiqubit gates and realizing quantum algorithms, Rev. Mod. Phys. **97**, 021003 (2025).

[42] S. Omanakuttan, A. Mitra, E. J. Meier, M. J. Martin, and I. H. Deutsch, Qudit entanglers using quantum optimal control, PRX Quantum **4**, 040333 (2023).

[43] S. Omanakuttan, V. Buchemmavari, J. A. Gross, I. H. Deutsch, and M. Marvian, Fault-tolerant quantum computation using large spin-cat codes, PRX Quantum **5**, 020355 (2024).

[44] J. R. Weggemans, A. Urech, A. Rausch, R. Spreeuw, R. Boucherie, F. Schreck, K. Schoutens, J. Minář, and F. Speelman, Solving correlation clustering with QAOA and a Rydberg qudit system: A full-stack approach, Quantum **6**, 687 (2022).

[45] A. Burshtein, S. Fraenkel, M. Goldstein, and R. Finkelstein, Robust control and entanglement of qudits in neutral atom arrays, Phys. Rev. Res. **8**, 013055 (2026).

[46] S. Taie, E. Ibarra-García-Padilla, N. Nishizawa, Y. Takasu, Y. Kuno, H.-T. Wei, R. T. Scalettar, K. R. A. Hazzard, and Y. Takahashi, Observation of antiferromagnetic correlations in an ultracold SU(N) Hubbard model, Nat. Phys. **18**, 1356 (2022).

[47] G. Pasqualetti, O. Bettermann, N. Darkwah Oppong, E. Ibarra-García-Padilla, S. Dasgupta, R. T. Scalettar, K. R. A. Hazzard, I. Bloch, and S. Fölling, Equation of state and thermometry of the 2D SU(N) Fermi-Hubbard model, Phys. Rev. Lett. **132**, 083401 (2024).

[48] M. Mancini, G. Pagano, G. Cappellini, L. Livi, M. Rider, J. Catani, C. Sias, P. Zoller, M. Inguscio, M. Dalmonte, and L. Fallani, Observation of chiral edge states with neutral fermions in synthetic Hall ribbons, Science **349**, 1510 (2015).

[49] B. K. Stuhl, H.-I. Lu, L. M. Aycock, D. Genkina, and I. B. Spielman, Visualizing edge states with an atomic Bose gas in the quantum Hall regime, Science **349**, 1514 (2015).

[50] T.-W. Zhou, G. Cappellini, D. Tusi, L. Franchi, J. Parravicini, C. Repellin, S. Greschner, M. Inguscio, T. Giamarchi, M. Filippone, J. Catani, and L. Fallani, Observation of universal Hall response in strongly interacting fermions, Science **381**, 427 (2023).

[51] R. Bücker, A. Perrin, S. Manz, T. Betz, C. Koller, T. Plisson, J. Rottmann, T. Schumm, and J. Schmiedmayer, Single-particle-sensitive imaging of freely propagating ultracold atoms, New J. Phys. **11**, 103039 (2009).

[52] A. Bergschneider, V. M. Klinkhamer, J. H. Becher, R. Klemt, G. Zürn, P. M. Preiss, and S. Jochim, Spin-resolved single-atom imaging of ^{6}Li in free space, Phys. Rev. A **97**, 063613 (2018).

[53] L. R. B. Picard, M. J. Mark, F. Ferlaino, and R. van Bijnen, Deep learning-assisted classification of site-resolved quantum gas microscope images, Meas. Sci. Technol. **31**, 025201 (2020).

[54] L. Su, A. Douglas, M. Szurek, A. H. Hébert, A. Krahn, R. Groth, G. A. Phelps, O. Marković, and M. Greiner, Fast single atom imaging for optical lattice arrays, Nat. Commun. **16**, 1017 (2025).

[55] D. S. Grün, S. J. M. White, A. Ortu, A. Di Carli, H. Edri, M. Lepers, M. J. Mark, and F. Ferlaino, Optical tweezer arrays of erbium atoms, Phys. Rev. Lett. **133**, 223402 (2024).

[56] A. M. Falconi, R. Panza, S. Sbernardori, R. Forti, R. Klemt, O. A. Karim, M. Marinelli, and F. Scazza, Microsecond-scale high-survival and number-resolved detection of ytterbium atom arrays, Phys. Rev. Lett. **135**, 203402 (2025).

[57] T. Mukaiyama, H. Katori, T. Ido, Y. Li, and M. Kuwata-Gonokami, Recoil-limited laser cooling of ^{87}Sr atoms near the Fermi temperature, Phys. Rev. Lett. **90**, 113002 (2003).

[58] J. Samland, S. Bennetts, C.-C. Chen, R. G. Escudero, F. Schreck, and B. Pasquiou, Optical pumping of $5s4d\,^1D_2$ strontium atoms for laser cooling and imaging, Phys. Rev. Res. **6**, 013319 (2024).

[59] L. Sonderhouse, C. Sanner, R. B. Hutson, A. Goban, T. Bilitewski, L. Yan, W. R. Milner, A. M. Rey, and J. Ye, Thermodynamics of a deeply degenerate SU(N)-symmetric Fermi gas, Nat. Phys. **16**, 1216 (2020).

[60] H. Ahmed, A. Litvinov, P. Guesdon, E. Maréchal, J.H. Huckans, B. Pasquiou, B. Laburthe-Tolra, and M. Robert-de-Saint-Vincent, Coherent control over the high-dimensional space of the nuclear spin of alkaline-earth atoms, PRX Quantum **6**, 020352 (2025).

[61] M. A. Norcia, A. W. Young, and A. M. Kaufman, Microscopic control and detection of ultracold strontium in optical-tweezer arrays, Phys. Rev. X **8**, 041054 (2018).

[62] A. Cooper, J. P. Covey, I. S. Madjarov, S. G. Porsev, M. S. Safronova, and M. Endres, Alkaline-earth atoms in optical tweezers, Phys. Rev. X **8**, 041055 (2018).

[63] H. Hwang, A. Byun, J. Park, S. de Léséleuc, and J. Ahn, Optical tweezers throw and catch single atoms, Optica **10**, 401 (2023).

[64] D. Bluvstein, H. Levine, G. Semeghini, T. T. Wang, S. Ebadi, M. Kalinowski, A. Keesling, N. Maskara, H. Pichler, M. Greiner, V. Vuletić, and M. D. Lukin, A quantum processor based on coherent transport of entangled atom arrays, Nature (London) **604**, 451 (2022).

[65] A. Pagano, D. Jaschke, W. Weiss, and S. Montangero, Optimal control transport of neutral atoms in optical tweezers at finite temperature, Phys. Rev. Res. **6**, 033282 (2024).

[66] L. Su, A. Douglas, M. Szurek, R. Groth, S. F. Ozturk, A. Krahn, A. H. Hébert, G. A. Phelps, S. Ebadi, S. Dickerson, F. Ferlaino, O. Marković, and M. Greiner, Dipolar quantum solids emerging in a Hubbard quantum simulator, Nature (London) **622**, 724 (2023).

[67] A. Browaeys and T. Lahaye, Many-body physics with individually controlled Rydberg atoms, Nat. Phys. **16**, 132 (2020).

[68] C. Gas-Ferrer, A. Rubio-Abadal, S. Buob, L. Bezzo, J. Höschele, and L. Tarruell, companion paper, Spin-resolved microscopy of ^{87}Sr SU(N) Fermi-Hubbard systems, Phys. Rev. X **16**, 041042 (2026).

[69] N. Q. Burdick, Y. Tang, and B. L. Lev, Long-lived spin-orbit-coupled degenerate dipolar Fermi gas, Phys. Rev. X **6**, 031022 (2016).

[70] A. Trautmann, P. Ilzhöfer, G. Durastante, C. Politi, M. Sohmen, M. J. Mark, and F. Ferlaino, Dipolar quantum mixtures of erbium and dysprosium atoms, Phys. Rev. Lett. **121**, 213601 (2018).

[71] M. Lecomte, A. Journeaux, J. Veschambre, J. Dalibard, and R. Lopes, Production and stabilization of a spin mixture of ultracold dipolar Bose gases, Phys. Rev. Lett. **134**, 013402 (2025).

[72] T. Plaßmann, L. Schäfer, M. Menashes, and G. Salomon, Rapid spin-resolved single-atom imaging of alkaline-earth fermions, [Dataset], Zenodo, 2026, https://doi.org/10.5281/zenodo.23234476.

[73] C. Tuchendler, A. M. Lance, A. Browaeys, Y. R. P. Sortais, and P. Grangier, Energy distribution and cooling of a single atom in an optical tweezer, Phys. Rev. A **78**, 033425 (2008).

[74] F. Pedregosa, G. Varoquaux, A. Gramfort, V. Michel, B. Thirion, O. Grisel, M. Blondel, P. Prettenhofer, R. Weiss, V. Dubourg, J. Vanderplas, A. Passos, D. Cournapeau, M. Brucher, M. Perrot, and E. Duchesnay, Scikit-learn: Machine learning in Python, J. Mach. Learn. Res. **12**, 2825 (2011).